Macho-Ortiz, A.; García Meca, C.; Fraile-Peláez, FJ.; Morant Pérez, M.; Llorente Sáez, R. (2016). Birefringence effects in multi-core fiber: coupled local-mode theory. Optics Express. 24(19):21415-21434. doi:10.1364/OE.24.021415.

Birefringence effects in multi-core fiber: coupled local-mode theory

ANDRÉS MACHO,[1,*] CARLOS GARCÍA-MECA,[1] F. JAVIER FRAILE-PELÁEZ,[2] MARIA MORANT,[1] AND ROBERTO LLORENTE[1]

[1]*Nanophotonics Technology Centre, Universitat Politècnica de València, Camino de Vera s/n, 46022 Valencia, Spain*
[2]*Dept. Teoría de la Señal y Comunicaciones, Universidad de Vigo E.I. Telecomunicación, Campus Universitario, E-36202 Vigo (Pontevedra), Spain*
**amachor@ntc.upv.es*

Abstract: In this paper, we evaluate experimentally and model theoretically the intra- and inter-core crosstalk between the polarized core modes in single-mode multi-core fiber media including temporal and longitudinal birefringent effects. Specifically, extensive experimental results on a four-core fiber indicate that the temporal fluctuation of fiber birefringence modifies the intra- and inter-core crosstalk behavior in both linear and nonlinear optical power regimes. To gain theoretical insight into the experimental results, we introduce an accurate multi-core fiber model based on local modes and perturbation theory, which is derived from the Maxwell equations including both longitudinal and temporal birefringent effects. Numerical calculations based on the developed theory are found to be in good agreement with the experimental data.

OCIS Codes: (060.0060) Fiber optics and optical communications; (060.2270) Fiber characterization; (060.2300) Fiber measurements; (060.4370) Nonlinear optics, fibers.

References and links

1. B. J. Puttnam, R. S. Luis, W. Klaus, J. Sakaguchi, J.-M. Delgado Mendinueta, Y. Awaji, N. Wada, Y. Tamura, T. Hayashi, M. Hirano, and J. Marciante, "2.15 Pb/s transmission using a 22 core homogeneous single-mode multi-core fiber and wideband optical comb," in Eur. Conf. Opt. Commun. (ECOC) (2015), paper PDP 3.1.
2. T. Mizuno, H. Takara, A. Sano, and Y. Miyamoto, "Dense space-division multiplexing transmission systems using multi-core and multi-mode fiber," J. Lightwave Technol. **34**(2), 582−591(2016).
3. M. Morant, A. Macho, and R. Llorente, "On the suitability of multicore fiber for LTE-advanced MIMO optical fronthaul systems," J. Lightwave Technol. **34**(2), 676−682 (2016).
4. T. Hayashi, T. Sasaki, E. Sasaoka, K. Saitoh, and M. Koshiba, "Physical interpretation of intercore crosstalk in multicore fiber: effects of macrobend, structure fluctuation, and microbend," Opt. Express **21**(5), 5401−5412 (2013).
5. J. M. Fini, B. Zhu, T. F. Taunay, M. F. Yan and K. S. Abedin, "Statistical models of multicore fiber crosstalk including time delays," J. Lightwave Technol. **30**(12), 2003–2010 (2012).
6. R. S. Luís, B. J. Puttnam, A. V. T. Cartaxo, W. Klaus, J. M. D. Mendinueta, Y. Awaji, N. Wada, T. Nakanishi, T. Hayashi, and T. Sasaki, "Time and modulation frequency dependence of crosstalk in homogeneous multi-core fibers," J. Lightwave Technol., **34**(2), pp. 441-447 (2016).
7. T. Hayashi, T. Taru, O. Shimakawa, T. Sasaki, and E. Sasaoka, "Characterization of crosstalk in ultra-low crosstalk multi-core fiber," J. Lightwave Technol. **30**(4), 583–589 (2012).
8. J. M. Fini, B. Zhu, T. F. Taunay, and M. F. Yan, "Statistics of crosstalk in bent multicore fibers," Opt. Express **18**(14), 15122–15129 (2010).
9. M. Koshiba, K. Saitoh, K. Takenaga, and S. Matsuo, "Multi-core fiber design and analysis: coupled-mode theory and coupled-power theory," Opt. Express **19**(26), B102–B111 (2011).
10. T. Hayashi, T. Taru, O. Shimakawa, T. Sasaki, and E. Sasaoka, "Design and fabrication of ultra-low crosstalk and low-loss multi-core fiber," Opt. Express **19**(17), 16576−16592 (2011).
11. M. Koshiba, K. Saitoh, K. Takenaga, and S. Matsuo, "Analytical expression of average power-coupling coefficients for estimating intercore crosstalk in multicore fibers," IEEE Photonics Journal **4**(5), 1987–1995 (2012).
12. A. Macho, M. Morant, and R. Llorente, "Experimental evaluation of nonlinear crosstalk in multi-core fiber," Opt. Express **23**(14), 18712–18720 (2015).
13. A. Macho, M. Morant, and R. Llorente, "Unified model of linear and nonlinear crosstalk in multi-core fiber," J. Lightwave Technol. **34**(13), 3035–3046 (2016).

14. A. Mecozzi, C. Antonelli, and M. Shtaif, "Coupled Manakov equations in multimode fibers with strongly coupled groups of modes," Opt. Express **20**(21), pp. 23436–23441 (2012).
15. A. Mecozzi, C. Antonelli, and M. Shtaif, "Nonlinear propagation in multi-mode fibers in the strong coupling regime," Opt. Express **20**(11), pp. 11673–11678 (2012).
16. S. Mumtaz, R. J. Essiambre, and G. P. Agrawal, "Nonlinear propagation in multimode and multicore fibers: generalization of the manakov equations," J. Lightwave Technol. **31**(3), 398–406 (2013).
17. S. Mumtaz, R.-J. Essiambre and G. P. Agrawal, "Birefringence effects in space-division multiplexed fiber transmission systems: Generalization of Manakov equation," in IEEE Photonics Society Summer Topical Meeting Series (IEEE, 2012), paper MC3.5.
18. L. Palmieri and A. Galtarossa, "Coupling effects among degenerate modes in multimode optical fibers," IEEE Photonics Journal 6(6), 0600408 (2014).
19. C. Antonelli, A. Mecozzi, and M. Shtaif, "The delay spread in fibers for SDM transmission: dependence on fiber parameters and perturbations," Opt. Express 23(3), pp. 2196–2202 (2015).
20. D. Marcuse, "Coupled-mode theory for anisotropic optical waveguides," Bell Syst. Technol. J., **54**(6), 985–995 (1975).
21. D. Wong, "Thermal stability of intrinsic stress birefringence in optical fibers," J. Lightwave Technol. **8**(11), 1757–1761 (1990).
22. D. Marcuse, *Theory of Dielectric Optical Waveguides* (Elsevier, 1974), Ch. 3.
23. D. Gloge, "Weakly guiding fibers," Applied Optics **10**(10), 2252–2258 (1971).
24. G. P. Agrawal, *Nonlinear Fiber Optics*, 5th ed. (Elsevier, 2013).
25. R. W. Boyd, *Nonlinear Optics*, 3rd ed. (Elsevier, 2008), Chap. 1.
26. A. M. Weiner, *Ultrafast Optics*, 1st ed. (John Wiley & Sons, 2009), Chap. 6.
27. A. V. T. Cartaxo, R. S. Luís, B. J. Puttnam, T. Hayashi, Y. Awaji, N. Wada, "Dispersion Impact on the Crosstalk Amplitude Response of Homogeneous Multi-Core Fibers," IEEE Phot. Technol. Letters, **28**(17), 1858−1861 (2016).
28. S. Huard, *Polarization of Light* (John Wiley & Sons, first edition), 1997, Chap. 2.
29. P. Drexler, and F. Pavel, "Optical Fiber Birefringence Effects – Sources, Utilization and Methods of Suppression," in *Recent Progress in Optical Fiber Research*, Yasin, M., Harun, S., and Arof, H. (eds.), (InTech, 2011), Chap. 7.
30. M. J. Weber, *Handbook of Optical Materials* (CRC University), 2003.
31. K. Iizuka, *Elements of Photonics Volume I* (Wiley-Interscience, first edition), 2002, Chap. 6.
32. C. D. Poole, D. L. Favin, "Polarization-mode dispersion measurements based on transmission spectra through a polarizer," J. Lightwave Technol. **12**(6), 917−929 (1994).
33. R. Hui, M. O'Sullivan, *Fiber Optic Measurement Techniques* (Elsevier, 2009), Chap. 4, pp. 420.
34. M. Karlsson, J. Brentel, and P. A. Andrekson, "Long-Term Measurement of PMD and Polarization Drift in Installed Fibers," J. Lightwave Technol. 18(7), 941 – 951 (2000).
35. M. Brodsky, N. J. Frigo, M. Boroditsky, and M. Tur, "Polarization Mode Dispersion of Installed Fibers," J. Lightwave Technol. 24(12), 4584 – 4599 (2006).

1. Introduction

Space-division multiplexing (SDM) using single-mode multi-core fibers (SM-MCFs) has attracted much attention over the last years to provide large fiber transmission capacity in backbone and access optical networks [1-3]. However, advanced SDM transmissions in polarization multiplexing SM-MCF systems should deal with the intra- and inter-core crosstalk impairment, which presents both a spatial and temporal stochastic nature induced by different effects. The spatial dependence of the crosstalk is induced by the longitudinal fiber perturbations as macrobending, microbending, and fiber twisting [4]. Moreover, the temporal dependence of the crosstalk is induced by: the relative delay between cores [5], the walk-off effect due to different group velocities between cores and referred to as the inter-core skew [6], changes in the state of polarization of the input signal [7] or the MCF temporal birefringence fluctuations.

In this topic, the spatial random nature of the crosstalk has been extensively investigated in [8-13] considering a single polarization and neglecting the intra-core coupling between orthogonal polarizations induced by the longitudinal random perturbations, which were heuristically inserted in the coupled-mode equations. On the other hand, in [14-17] the Manakov equations have been extended to multi-mode fibers (MMFs) and multi-mode multi-core fibers (MM-MCFs) to analyze linear and nonlinear propagation in SDM systems modeling intra- and inter-core coupling effects. In addition, in [18,19] the mode coupling has also been theoretically investigated in MMFs and MM-MCFs considering both orthogonal

polarizations and the longitudinal random perturbations of the fiber. In [18] the bending and twisting of the media were modeled in the coupling matrix (composed by the coupling coefficients of the coupled-mode theory proposed in [20] for anisotropic optical waveguides), and in [19] the spatial random perturbations were included in the propagation matrix of the optical media. In all these previous works [8-19], the longitudinal perturbations of the fiber have been described assuming ideal modes but omitting the temporal fluctuations of the SDM fiber perturbations.

Furthermore, the temporal dependence of the crosstalk in SM-MCFs due to the relative delay between cores, the inter-core skew and changes in the state of polarization of the input signal has been investigated in [5-7] including the fiber perturbations in the coupled-mode theory using a heuristic formalism and omitting intra-core and nonlinear effects. In addition, the temporal fiber birefringence fluctuation inducing crosstalk temporal dependence has not been investigated so far in SM-MCFs.

This paper reports on the theoretical and experimental investigation of the temporal MCF birefringence effects and longitudinal random perturbations and their impact on the intra- and inter-core crosstalk in SM-MCFs using a more rigorous formalism. In particular, aimed to accurately describe linear and nonlinear intra- and inter-core coupling effects in SM-MCFs including both longitudinal and temporal MCF perturbations, we propose and develop a coupled local-mode theory (CLMT) considering these random perturbations in the Maxwell equations from the onset. As a result, we obtain an accurate fiber model able to predict the different types of crosstalk between the polarized core modes (PCMs) in SM-MCFs: (i) the intra-core crosstalk (iC-XT) which describes the mode coupling between orthogonal polarizations in a given core; (ii) the direct inter-core crosstalk (DIC-XT) modeling the mode coupling between the same polarization axis in different cores; and (iii) the cross inter-core crosstalk (XIC-XT) involving mode coupling between orthogonal polarizations in different cores. To complete our study, we perform extensive experimental measurements on a four-core fiber, which are found to be in good agreement with numerical simulations based on the proposed CLMT theory. Considering that in previous works [7-13] the crosstalk in MCF is usually estimated calculating the mean of the random process, our investigations are mainly focused on the behavior of the crosstalk mean between the PCMs.

The paper is structured as follows. In Section 2, the aforementioned coupled local-mode theory is derived from the Maxwell equations. In Section 3, the fiber simulation model is described and extensive numerical simulations are performed considering lowly- and highly-birefringent (LB and HB) cores. The temporal evolution of the MCF random birefringence and its impact on the mean of the linear and nonlinear iC-, DIC- and XIC-XT is also reported. The experimental validation of the theoretical model is performed in Section 4 on a homogeneous four-core fiber (4CF). Finally, in Section 5 the main conclusions of this work are highlighted.

2. Coupled local-mode theory

Coupled local-mode theory (CLMT) for SM-MCF media including both temporal and longitudinal birefringent effects in the Maxwell equations is reported in this section. As depicted in Fig.1, in a real two-core MCF, each core $m = a,b$ can be modeled as a series of birefringent segments with a different time-varying retardation and random orientation of the local principal axes. Therefore, the first-order electrical susceptibility tensor $\chi_{ij}^{(1)}$ can slightly fluctuate along the fiber, as a consequence of external perturbations such as bending, twisting, and temperature variations, as well as due to manufacturing imperfections [4,21]. As a result, in each segment of a given core m, the propagation constant of the PCMs LP_{01x} and LP_{01y} presents a different value due to the mentioned slight changes, and therefore, the transversal function of each PCM "mi" ($i = x,y$) is also modified.

In order to model theoretically this scenario, the concept of local mode is included in the classical perturbation theory [22]. A local mode can be defined as an eigenfunction in a short core segment where the propagation constant and the transversal Bessel function [23] are approximately invariant. Hence, each core can be separated in different segments and

local modes where the longitudinal and temporal birefringence conditions are approximately constant.

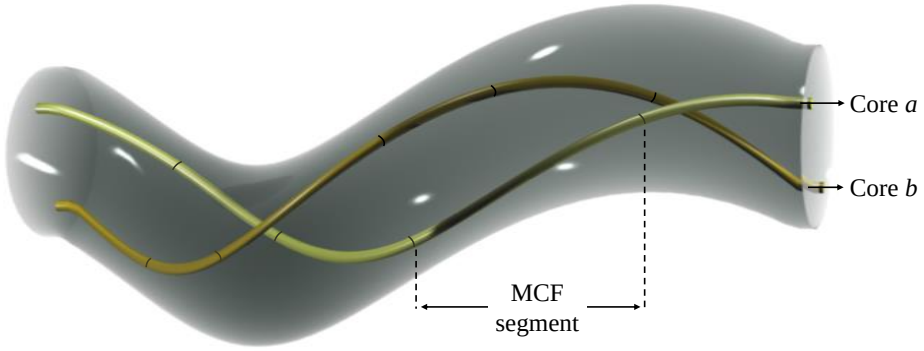

Fig. 1: Multi-core fiber comprising different birefringent segments in cores *a* and *b* with longitudinal and temporal varying fluctuations in the refractive index tensor.

In this way, in contrast with [4-13] where the longitudinal and temporal MCF perturbations are heuristically inserted in the coupled-mode theory assuming ideal modes, we include the longitudinal and temporal MCF random perturbations in the Maxwell equations considering local modes. The resulting coupled local-mode equations include oscillatory terms and mode-coupling coefficients (MCCs), which are longitudinal and temporal dependent. This CLMT formalism will allow us to model the impact of the different longitudinal and temporal fiber random perturbations on the crosstalk among the different PCMs and find the predominant linear and nonlinear MCCs describing iC-XT, DIC-XT and XIC-XT.

2.1 Nonlinear coupled wave equations

Our initial goal is to include the MCF random perturbations in the theoretical analysis from the Maxwell equations. We start by analyzing the coupled wave equations of an anisotropic and nonlinear SM-MCF. Considering monochromatic electric fields with both orthogonal polarizations and slowly varying amplitude functions, the real wave function of the global electric field ($\mathcal{E}$), the linear polarization ($\mathcal{P}^{(1)}$) and the nonlinear polarization ($\mathcal{P}^{(3)}$) of a weakly guiding MCF can be written as [24-26]:

$$\vec{\mathcal{E}}\left(\vec{r},t\right)=\sum_{i=x,y}\frac{1}{2}\left[E_{i,\omega_0}\left(\vec{r};t\right)\exp\left(j\omega_0 t\right)+c.c.\right]\hat{u}_i, \tag{1a}$$

$$\vec{\mathcal{P}}^{(1)}\left(\vec{r},t\right)=\sum_{i=x,y}\frac{1}{2}\left[P^{(1)}_{i,\omega_0}\left(\vec{r};t\right)\exp\left(j\omega_0 t\right)+c.c.\right]\hat{u}_i, \tag{1b}$$

$$\vec{\mathcal{P}}^{(3)}\left(\vec{r},t\right)\approx\sum_{i=x,y}\frac{1}{2}\left[P^{(3)}_{i,\omega_0}\left(\vec{r};t\right)\exp\left(j\omega_0 t\right)+c.c.\right]\hat{u}_i, \tag{1c}$$

where $E_{i,\omega 0}$, $P_{i,\omega 0}{}^{(1)}$ and $P_{i,\omega 0}{}^{(3)}$ are the complex amplitudes, ω_0 is the angular frequency of the optical carrier and *c.c.* are the complex conjugate terms. In this work, the semicolon symbol in Eqs. (1) is used to separate the rapid temporal oscillation of the optical carrier from the slow temporal evolution of the complex amplitudes modeling temporal birefringence fluctuations or additional temporal variations as the fluctuation of the state of polarization of the input signal. Although the MCF dispersive effects inducing crosstalk time dependence [27] have been omitted in Eqs. (1) when assuming monochromatic electric fields, they will be discussed at the end of section 2.3. In addition, the complex amplitude vector $P_{i,3\omega 0}{}^{(3)}$ of the nonlinear polarization in $3\omega_0$ was omitted, taking into account that the phase-matching condition in this nonlinear term is not satisfied in silica fibers [24]. The complex amplitude of the linear and nonlinear polarizations can be expressed as [25]:

$$P_{i,\omega_0}^{(1)}\left(\vec{r};t\right)=\varepsilon_0\chi_{ij}^{(1)}\left(z;t\right)E_{j,\omega_0}\left(\vec{r};t\right), \tag{2a}$$

$$P_{i,\omega_0}^{(3)}\left(\vec{r};t\right)=\frac{3}{4}\varepsilon_0\chi_{ijkl}^{(3)}\left(-\omega_0;\omega_0,\omega_0,-\omega_0\right)E_{j,\omega_0}\left(\vec{r};t\right)E_{k,\omega_0}\left(\vec{r};t\right)E_{l,-\omega_0}\left(\vec{r};t\right), \tag{2b}$$

where the first-order electrical susceptibility tensor $\chi_{ij}^{(1)}$ is assumed longitudinal and temporal dependent due to the MCF perturbations. Moreover, the third-order susceptibility $\chi_{ijkl}^{(3)}$ can be approximated in silica media to [26]:

$$\chi_{ijkl}^{(3)}\left(-\omega_0;\omega_0,\omega_0,-\omega_0\right)=\frac{1}{3}\chi_{xxxx}^{(3)}\left(-\omega_0;\omega_0,\omega_0,-\omega_0\right)\cdot\left(\delta_{ij}\delta_{kl}+\delta_{ik}\delta_{jl}+\delta_{il}\delta_{jk}\right), \tag{3}$$

where $\chi_{xxxx}^{(3)}=\chi_{ijkl}^{(3)}$ with $i=j=k=l=x$ and δ_{ij} is the Kronecker delta function defined as $\delta_{ij}=1$ when $i=j$ and $\delta_{ij}=0$ otherwise.

From the first and second Maxwell equations (Ampère's and Faraday's laws) in the time domain and using Eqs. (1)-(3), the nonlinear coupled wave equations for the complex amplitudes are found to be:

$$\begin{aligned}&\Delta E_{x,\omega_0}\left(\vec{r};t\right)+k_0^2\left[\varepsilon_{r,x}\left(\vec{r};t\right)E_{x,\omega_0}\left(\vec{r};t\right)+\sigma\left(\vec{r};t\right)E_{y,\omega_0}\left(\vec{r};t\right)\right]\\&\quad+k_0^2\gamma\left[\left(\left|E_{x,\omega_0}\left(\vec{r};t\right)\right|^2+\frac{2}{3}\left|E_{y,\omega_0}\left(\vec{r};t\right)\right|^2\right)E_{x,\omega_0}\left(\vec{r};t\right)+\frac{1}{3}E_{y,\omega_0}^2\left(\vec{r};t\right)E_{x,-\omega_0}\left(\vec{r};t\right)\right]=0,\end{aligned} \tag{4a}$$

$$\begin{aligned}&\Delta E_{y,\omega_0}\left(\vec{r};t\right)+k_0^2\left[\varepsilon_{r,y}\left(\vec{r};t\right)E_{y,\omega_0}+\sigma\left(\vec{r};t\right)E_{x,\omega_0}\right]\\&\quad+k_0^2\gamma\left[\left(\left|E_{y,\omega_0}\left(\vec{r};t\right)\right|^2+\frac{2}{3}\left|E_{x,\omega_0}\left(\vec{r};t\right)\right|^2\right)E_{y,\omega_0}\left(\vec{r};t\right)+\frac{1}{3}E_{x,\omega_0}^2\left(\vec{r};t\right)E_{y,-\omega_0}\left(\vec{r};t\right)\right]=0,\end{aligned} \tag{4b}$$

where Δ is the Laplacian operator; $\varepsilon_{r,i}=1+\chi_{ii}^{(1)}$; $\sigma=\chi_{xy}^{(1)}$; $\gamma=0.75\cdot\chi_{xxxx}^{(3)}$; $k_0=\omega_0/c_0$ is the wavenumber at the vacuum and $E_{i,-\omega0}=(E_{i,\omega0})^*$, where * denotes complex conjugation. Note that we have assumed in Eq. (4b) that $\chi_{xy}^{(1)}=\chi_{yx}^{(1)}$ in order to satisfy the Poynting theorem [28] when considering monochromatic electric fields in silica media.

Now, in order to simplify the mathematical discussion and without loss of generality, we consider a MCF comprising two cores *a* and *b*. Thus, the relative electric permittivity of the MCF $\varepsilon_{r,i}$ is defined in each polarization axis $i=x,y$ as (we use the symbol := to indicate definition):

$$\begin{aligned}\varepsilon_{r,i}\left(\vec{r};t\right)&:=\varepsilon_{r,ci}\left(\vec{r};t\right)+\Delta\varepsilon_{r,ai}\left(\vec{r};t\right)+\Delta\varepsilon_{r,bi}\left(\vec{r};t\right)=\\&=\begin{cases}\vec{r}\equiv\text{core }a\text{:} & \varepsilon_{r,ai}\left(z;t\right)=\varepsilon_{r,ci}\left(z;t\right)+\Delta\varepsilon_{r,ai}\left(z;t\right)=n_{ai}^2\left(z;t\right)\\\vec{r}\equiv\text{cladding:} & \varepsilon_{r,ci}\left(z;t\right)=n_{ci}^2\left(z;t\right)\\\vec{r}\equiv\text{core }b\text{:} & \varepsilon_{r,bi}\left(z;t\right)=\varepsilon_{r,ci}\left(z;t\right)+\Delta\varepsilon_{r,bi}\left(z;t\right)=n_{bi}^2\left(z;t\right)\end{cases}\end{aligned} \tag{5}$$

where $\varepsilon_{r,ai}$, $\varepsilon_{r,bi}$ and $\varepsilon_{r,ci}$ are the relative electric permittivity in the cores *a*, *b* and in the cladding, respectively; $\Delta\varepsilon_{r,ai}$ and $\Delta\varepsilon_{r,bi}$ are the difference between the relative electric permittivity of the cladding and those of cores *a* and *b*, respectively; and n_{ai}, n_{bi} and n_{ci} are the refractive index in each polarization axis in cores *a*, *b* and in the cladding region, respectively, considering both LB- and HB-MCFs. The linear birefringence is observed when $\varepsilon_{r,x}\neq\varepsilon_{r,y}$ and the circular birefringence is given by:

$$\sigma\left(\vec{r};t\right):=\begin{cases}\vec{r}\equiv\text{core }a\text{:} & \sigma_a\left(z;t\right)=\chi_{a,xy}^{(1)}\left(z;t\right)\\\vec{r}\equiv\text{cladding:} & \sigma_c\left(z;t\right)=\chi_{c,xy}^{(1)}\left(z;t\right)\\\vec{r}\equiv\text{core }b\text{:} & \sigma_b\left(z;t\right)=\chi_{b,xy}^{(1)}\left(z;t\right)\end{cases} \tag{6}$$

Furthermore, considering the low nonlinear nature of silica media, the nonlinear parameter γ is assumed constant in each dielectric region of the MCF.

2.2 Coupled local-mode equations

From the perturbation theory [22], the electric field of Eqs. (4) can be approximated in the MCF media as ($i = x,y$):

$$E_{i,\omega_0}(\vec{r};t) \approx \sum_{m=a,b} E_{mi,\omega_0}(\vec{r};t) = \sum_{m=a,b} A_{mi}(z;t)\,F_{mi}(x,y;z,t)\exp\left[-j\Phi_{mi}(z;t)\right], \tag{7}$$

where E_{mi} is the complex amplitude of the electric field of the PCM *"mi"* considering isolated cores; A_{mi} is the complex envelope; F_{mi} is the transversal local eigenfunction which can be calculated using the equivalent refractive index $n_{mi}^{(eq)}$ of the PCM *"mi"* as detailed in the Appendix; and Φ_{mi} is the complex phase function modeling MCF longitudinal random perturbations, temporal birefringence effects and optical attenuation:

$$\Phi_{mi}(z;t) := \phi_{mi}(z;t) - j\frac{1}{2}\alpha z, \tag{8a}$$

where α is the power attenuation coefficient of the MCF (assumed similar in each PCM), and ϕ_{mi} is the real phase function involving the longitudinal and temporal MCF perturbations:

$$\phi_{mi}(z;t) := \int_0^z \beta_{mi}^{(eq)}(\delta;t)\,d\delta = \beta_{mi} z + \int_0^z \beta_{mi}^{(B)}(\delta;t) + \beta_{mi}^{(S)}(\delta;t)\,d\delta. \tag{8b}$$

Here, β_{mi} is the unperturbed phase constant of the polarized core mode "*mi*"; $\beta_{mi}^{(B)}$ is the phase perturbation modeling macrobends; and $\beta_{mi}^{(S)}$ is the phase perturbation including structural fluctuations induced by microbending, twisting, temporal fiber birefringence and additional temporal variations as the fluctuation of the state of polarization of the laser. It should be noted that the functions A_{mi}, F_{mi} and Φ_{mi} also depend on the angular frequency ω_0. However, considering monochromatic electric fields the frequency dependence has been omitted in the notation.

Furthermore, as it was pointed out previously, the F_{mi} function is assumed longitudinal dependent. Considering that the phase function Φ_{mi} is modified along the MCF length, the transversal function F_{mi} should also be modified along the longitudinal direction of the fiber. Hence, assuming the function $F_{mi}(x,y;z,t)\cdot\exp(-j\Phi_{mi}(z;t))$ as local eigenmode in $\Delta z \geq \lambda$, the following Helmholtz equation should be satisfied in each *"mi"* polarized core mode:

$$\Delta\left[F_{mi}(x,y;z,t)\exp\left(-j\Phi_{mi}(z;t)\right)\right] + k_0^2\varepsilon_{r,mi}(\vec{r};t)\left[F_{mi}(x,y;z,t)\exp\left(-j\Phi_{mi}(z;t)\right)\right] = 0; \tag{9}$$

Therefore, using Eq. (5) and assuming that $\partial_z F_{mi} \approx 0$ and $\partial_z^2 F_{mi} \approx 0$ in $\Delta z \approx \lambda$, we obtain the following relation:

$$\begin{aligned}\Delta_T F_{ai}(x,y;z,t) + k_0^2\varepsilon_{r,i}(\vec{r};t)F_{ai}(x,y;z,t) = \\ = \left[k_0^2\Delta\varepsilon_{r,bi}(\vec{r};t) + j\partial_z\beta_{ai}^{(eq)}(z;t) + \left(\beta_{ai}^{(eq)}(z;t)\right)^2 - j\alpha\beta_{ai}^{(eq)}(z;t)\right]F_{ai}(x,y;z,t),\end{aligned} \tag{10}$$

where $\Delta_T = \partial_x^2 + \partial_y^2$ is the transverse Laplacian operator. A similar expression is found for the polarized core mode *bi* exchanging '*a*' by '*b*' in Eq. (10). Now, substituting the global electric field given by Eq. (7) into the nonlinear coupled wave equations Eqs. (4) using Eq. (10), considering the slowly varying envelope approximation with $\partial_z^2 A_{mi} \approx 0$ in $\Delta z \approx \lambda$, multiplying by the respective $F_{mi}(x,y;z,t)\cdot\exp(+j\phi_{mi}(z;t))$ and integrating in an infinite cross-section area of the MCF (as indicated in [22] for the classical derivation of the perturbation theory), we obtain the following coupled local-mode equation:

$$
\begin{aligned}
j\partial_z A_{ax}(z;t) = {} & c_{ax}(z;t)A_{ax}(z;t) + m_{ax,ay}(z;t)\exp\left(-j\Delta\phi_{ay,ax}(z;t)\right)A_{ay}(z;t) \\
& + \exp\left(-j\Delta\phi_{bx,ax}(z;t)\right)\left[k_{ax,bx}(z;t) - j\chi_{ax,bx}(z;t)\partial_z\right]A_{bx}(z;t) \\
& + \eta_{ax,by}(z;t)\exp\left(-j\Delta\phi_{by,ax}(z;t)\right)A_{by}(z;t) \\
& + \exp(-\alpha z)\left[q_{ax}(z;t)\left|A_{ax}(z;t)\right|^2 + g_{ax}(z;t)\left|A_{ay}(z;t)\right|^2\right]A_{ax}(z;t) \\
& + \frac{1}{2}\exp(-\alpha z)g_{ax}(z;t)\exp\left(-j2\Delta\phi_{ay,ax}(z;t)\right)A_{ax}^{*}(z;t)A_{ay}^{2}(z;t),
\end{aligned}
\tag{11}
$$

where c_{ax}, $m_{ax,ay}$, $k_{ax,bx}$, $\chi_{ax,bx}$, $\eta_{ax,by}$, q_{ax} and g_{ax} are the mode-coupling coefficients (MCCs) defined in the next subsection; and the mismatching functions are defined as $\Delta\phi_{ay,ax} := \phi_{ay} - \phi_{ax}$, $\Delta\phi_{bx,ax} := \phi_{bx} - \phi_{ax}$ and $\Delta\phi_{by,ax} := \phi_{by} - \phi_{ax}$. It should be noted that the theoretical model is completed by three additional coupled local-mode equations for the *ay*, *bx* and *by* polarized core modes, which can be obtained just by exchanging the corresponding subindexes in Eq. (11). It is worth mentioning that additional nonlinear terms modeling cross-coupling effects should be included in Eq. (11) for coupled MCFs with a core pitch value (d_{ab}) lower than three times the core radius (R_0). However, if we assume a MCF with $d_{ab} >> 3R_0$, the self-coupling effect is the predominant nonlinear coupling effect and the additional nonlinear terms can be neglected [13].

2.3 Linear and nonlinear mode-coupling coefficients

The linear MCCs of the coupled local-mode equation Eq. (11) are defined as:

$$
\chi_{ax,bx}(z;t) := \frac{\beta_{bx}^{(\mathrm{eq})}(z;t)}{\beta_{ax}^{(\mathrm{eq})}(z;t)N_{ax}(z;t)}\iint F_{ax}(x,y;z,t)F_{bx}(x,y;z,t)\,dS_{\infty}, \tag{12a}
$$

$$
c_{ax}(z;t) := \frac{k_0^2}{2\beta_{ax}^{(\mathrm{eq})}(z;t)N_{ax}(z;t)}\iint \Delta\varepsilon_{r,bx}(z;t)F_{ax}^2(x,y;z,t)\,dS_{\infty}, \tag{12b}
$$

$$
m_{ax,ay}(z;t) := \frac{k_0^2}{2\beta_{ax}^{(\mathrm{eq})}(z;t)N_{ax}(z;t)}\iint \sigma(\vec{r};t)F_{ax}(x,y;z,t)F_{ay}(x,y;z,t)\,dS_{\infty}, \tag{12c}
$$

$$
k_{ax,bx}(z;t) := \frac{k_0^2}{2\beta_{ax}^{(\mathrm{eq})}(z;t)N_{ax}(z;t)}\iint \Delta\varepsilon_{r,ax}(z;t)F_{ax}(x,y;z,t)F_{bx}(x,y;z,t)\,dS_{\infty}, \tag{12d}
$$

$$
\begin{aligned}
\eta_{ax,by}(z;t) &:= \frac{k_0^2}{2\beta_{ax}^{(\mathrm{eq})}(z;t)N_{ax}(z;t)}\iint \sigma(\vec{r};t)F_{ax}(x,y;z,t)F_{by}(x,y;z,t)\,dS_{\infty} \\
&\approx \frac{k_0^2}{2\beta_{ax}^{(\mathrm{eq})}(z;t)N_{ax}(z;t)}\left[\begin{array}{l}\sigma_b(z;t)\iint F_{ax}(x,y;z,t)F_{by}(x,y;z,t)\,dS_b \\ +\sigma_a(z;t)\iint F_{ax}(x,y;z,t)F_{by}(x,y;z,t)\,dS_a\end{array}\right],
\end{aligned}
\tag{12e}
$$

with [29]:

$$
\sigma_{a(b)}(z) \approx \pi R_0 f_{\mathrm{T}}(z) n_{a(b)}^4 \left|p_{11} - p_{12}\right|, \tag{13}
$$

$$
n_{a(b)} = \left(n_{ax(bx)} + n_{ay(by)}\right)\Big/2, \tag{14}
$$

where f_{T} is the twist rate along the MCF length; p_{11} and p_{12} are components of the photo-elastic tensor [30]; and $n_{a(b)}$ is the average value of the material refractive index of each core excluding temporal birefringence fluctuation. It should be remarked that considering the temporal birefringence random fluctuation of $n_{a(b)}$ of the order of $\sim 10^{-7}$ (as it is experimentally verified in Section 4), this fluctuation can be neglected when $n_{a(b)}$ is raised to the fourth power in Eq. (13). In addition, the nonlinear MCCs are given by the expressions (in $\mathrm{W}^{-1}\cdot\mathrm{m}^{-1}$):

$$q_{ax}(z;t) \coloneqq \frac{k_0^2}{2\beta_{ax}^{(\mathrm{eq})}(z;t)\,N_{ax}(z;t)} \iint \gamma F_{ax}^4(x,y;z,t)\,dS_\infty, \tag{15a}$$

$$g_{ax}(z;t) \coloneqq \frac{k_0^2}{3\beta_{ax}^{(\mathrm{eq})}(z;t)\,N_{ax}(z;t)} \iint \gamma F_{ax}^2(x,y;z,t)\,F_{ay}^2(x,y;z,t)\,dS_\infty, \tag{15b}$$

where $N_{ax}(z;t) \coloneqq \iint F_{ax}^2(x,y;z,t)dS_\infty$; S_∞ is the infinite cross-sectional area of the MCF; and $S_{a(b)}$ is the cross-sectional area of each core. It should be noted that, in coherence with [18], the longitudinal random perturbations of the fiber are included in the MCCs. Nevertheless, in our method we have considered not only longitudinal perturbations, but also temporal ones. As a result, the derived MCCs are found to be time dependent. Moreover, note that our model inherently incorporates these stochastic perturbations, as they were directly included in the Maxwell equations. Specifically, they also appear in the exponential terms of Eq. (11), which account for possible slight changes in the longitudinal or temporal birefringent conditions.

The linear MCCs $\chi_{ax,bx}$, c_{ax} and $k_{ax,bx}$ are similar to the linear MCCs investigated in [13], where it was observed that $k_{ax,bx}$ is the predominant linear MCC and that $\chi_{ax,bx}$ and c_{ax} can be neglected. However, if polarization effects are included in the Maxwell equations, two new linear MCCs appear, $m_{ax,ay}$ and $\eta_{ax,by}$, which model the iC-XT and XIC-XT, respectively. In order to investigate whether these coefficients should be maintained in Eq. (11) when compared with $k_{ax,bx}$, the ratios $m_{ax,ay}/k_{ax,bx}$ and $\eta_{ax,by}/k_{ax,bx}$ are analyzed following a similar procedure to the one discussed in [13].

Assuming a straight MCF with constant twist rate f_T and without temporal birefringence, the linear MCCs $m_{ax,ay}$ and $\eta_{ax,by}$ are found to be only longitudinal dependent and are maximized when considering homogeneous PCMs with $n_{ai} = n_{bi}$ ($i = x,y$) and $F_{ax(bx)} = F_{ay(by)}$. As a result, the spatial average of the ratios $\langle m_{ax,ay}(z)/k_{ax,bx}(z)\rangle$ and $\langle \eta_{ax,by}(z)/k_{ax,bx}(z)\rangle$ can be calculated from Eqs. (12) with a similar derivation as in [13]:

$$\left\langle \frac{m_{ax,ay}(z)}{k_{ax,bx}(z)} \right\rangle \approx \frac{\sigma_a}{2\left(n_a^2 - n_c^2\right)} \frac{u_a\left[J_0^2(u_a) + J_1^2(u_a)\right]}{J_0(u_a)\,J_1(u_a)} \frac{K_0(w_b)}{K_0(w_b d_{ab}/R_0)}, \tag{16a}$$

$$\left\langle \frac{\eta_{ax,by}(z)}{k_{ax,bx}(z)} \right\rangle \approx \frac{1}{\left(n_a^2 - n_c^2\right)} \left[\sigma_b \frac{u_a}{u_b} \frac{J_0(u_a)}{J_0(u_b)} \frac{J_1(u_b)}{J_1(u_a)} \frac{K_0(w_b)}{K_0(w_a)} \frac{K_0(w_a d_{ab}/R_0)}{K_0(w_b d_{ab}/R_0)} + \sigma_a \right] \approx \frac{\sigma_b + \sigma_a}{n_a^2 - n_c^2}, \tag{16b}$$

where R_0 is the core radius, n_c is the cladding refractive index and the modal parameters $u_{a(b)}$ and $w_{a(b)}$ are given by [23]. As an example, the ratios given by Eqs. (16) are calculated assuming an ideal straight homogeneous two-core fiber with parameters: $n_{a(b)} = 1.45$, $n = 1.44$, $\lambda = 1550$ nm, $R_0 = 4$ μm.

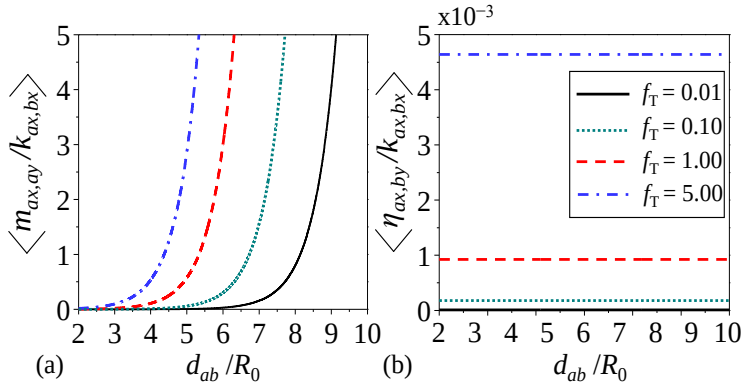

Fig. 2: Comparison of the linear mode-coupling coefficients (MCCs) $m_{ax,ay}$ and $\eta_{ax,by}$ with the linear MCC $k_{ax,bx}$ using the spatial average ratios given by Eqs. (16) for different constant twist rate values f_T and core pitch ratio d_{ab}/R_0: (a) $\langle m_{ax,ay}/k_{ax,bx}\rangle$ and (b) $\langle \eta_{ax,by}/k_{ax,bx}\rangle$. (Legend shown on Fig. 2(b) also applies to Fig. 2(a)).

Figure 2 shows the behavior of the calculated ratios for different constant twist rate values f_T and different values of the ratio between the core pitch and the core radius d_{ab}/R_0. From Fig. 2(a), it can be noted that $m_{ax,ay}$ should be maintained in Eq. (11), since this MCC is usually of the same order or higher than $k_{ax,bx}$. As expected, the higher the twist rate value f_T, the higher the mode coupling between the *x* and *y* orthogonal polarizations in a given core. However, as depicted in Fig. 2(b), the linear MCC $\eta_{ax,by}$ can be neglected in Eq. (11) for any core pitch value. Hence, the XIC-XT will depend directly on the iC-XT of both cores, as verified in next sections. Note that the MCC analysis considering heterogeneous cores with $n_a \neq n_b$ is not included in Fig. 2 because the conclusions in the predominant linear MCCs are found to be identical.

As a result, redefining the complex envelopes as $A(z;t) := \mathcal{A}(z;t)\exp(\alpha z/2)$ and considering all adjacent cores to core *a* in a *N*-core MCF, the final expression of the coupled local-mode equation for the polarized core mode *ax* including linear and nonlinear intra- and inter-core crosstalk in MCF media with $d_{ab} > 3R_0$ is given by the expression:

$$\begin{aligned} j\left(\partial_z + \frac{\alpha}{2}\right)\mathcal{A}_{ax}(z;t) &= m_{ax,ay}(z;t)\exp\left(-j\Delta\phi_{ay,ax}(z;t)\right)\mathcal{A}_{ay}(z;t) \\ &+ \sum_{\delta=b}^{N} k_{ax,\delta x}(z;t)\exp\left(-j\Delta\phi_{\delta x,ax}(z;t)\right)\mathcal{A}_{\delta x}(z;t) \\ &+ \left(q_{ax}(z;t)\left|\mathcal{A}_{ax}(z;t)\right|^2 + g_{ax}(z;t)\left|\mathcal{A}_{ay}(z;t)\right|^2\right)\mathcal{A}_{ax}(z;t) \\ &+ \frac{1}{2}g_{ax}(z;t)\exp\left(-j2\Delta\phi_{ay,ax}(z;t)\right)\mathcal{A}_{ax}^{*}(z;t)\mathcal{A}_{ay}^{2}(z;t). \end{aligned} \tag{17}$$

Furthermore, considering non-monochromatic electric fields in Eqs. (1) and performing a similar mathematical discussion from the Maxwell equations, the CLMT can also be used to describe optical pulse propagation in SM-MCFs including inside the brackets of the left-hand side of Eq. (17) the dispersion operator $\hat{D}_{t,ax}$ defined as $\hat{D}_{t,ax} := \sum_{k=1}^{\infty}(-j)^{k-1}\beta_{ax}^{(k)}\partial_t^k/k!$, where $\beta_{ax}^{(k)} := \partial_\omega^k \beta_{ax}(\omega_0)$. In addition, the inter-core skew and the additional dispersive effects inducing a crosstalk time dependence [6,27] can also be modeled via this dispersion operator. However, the fiber dispersion effects are omitted in this work in order to evaluate only the time dependence of the crosstalk induced by the temporal birefringence fluctuations of the MCF, as it was pointed out previously. Alternatively to the CLMT, the theoretical models reported in [14-19] can also be extended to describe the temporal perturbations of the optical media inducing a crosstalk time dependence in MMFs and MM-MCFs.

3. Equivalent refractive index model and numerical simulations

In this section, the MCF simulation model is detailed and extensive numerical simulations of the crosstalk mean between the PCMs are performed considering temporal and longitudinal birefringent effects of the optical media. We observe that the temporal birefringence fluctuation of each core modifies the average value of the iC-, DIC- and XIC-XT. In addition, fiber twisting is proposed as a strategy of birefringence management to balance the inter-core crosstalk between the PCMs of different cores.

3.1 Equivalent refractive-index model with longitudinal and temporal perturbations

In a given core *m* of a SM-MCF, the longitudinal and temporal perturbations of the MCF should be included in the equivalent refractive index $n_{mi}^{(eq)}$ of each "*mi*" polarized core mode ($LP_{01,mx}$ and $LP_{01,my}$). This index determines the value of the ϕ_{mi} and F_{mi} functions, as well as of the mode-coupling coefficients. In turn, these coefficients can be obtained via numerical integration of Eqs. (12) and (15) or through the closed-form expressions reported in [13] together with Eq. (16a) (substituting the material refractive index n_a by $n_{ax}^{(eq)}$). Furthermore,

the ϕ_{mi} functions can be approximated in a short MCF segment, where the longitudinal MCF random perturbations are assumed to be approximately constant, as:

$$\phi_{mi}(z;t)=\int_{z_1}^{z_2}\beta_{mi}^{(\mathrm{eq})}(\xi;t)\,d\xi\approx\beta_{mi}^{(\mathrm{eq})}(z;t)\cdot(z_2-z_1)=k_0 n_{mi}^{(\mathrm{eq})}(z;t)\cdot(z_2-z_1). \tag{18}$$

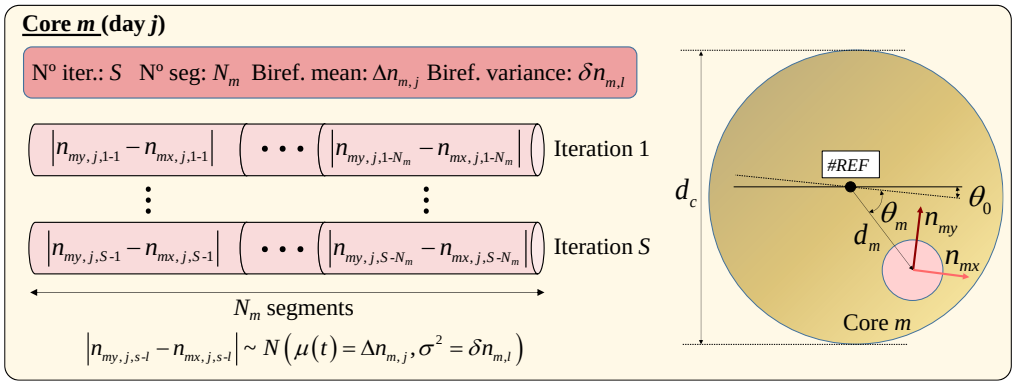

Fig. 3. Multi-core fiber simulation model including longitudinal perturbations and temporal birefringence effects.

Hence, the ϕ_{mi} functions, MCCs and the coupled local-mode equations can be numerically solved by using the proper expression for $n_{mi}^{(\mathrm{eq})}(z;t)$, which should include the longitudinal and temporal MCF perturbations. In [10], the equivalent refractive index model was proposed assuming a single polarization and without including temporal birefringence effects. Here, in order to simulate also a slowly varying longitudinal and temporal MCF birefringence fluctuation in a time period spanning several days, we extend the equivalent refractive index model of [10] as depicted in Fig. 3.

In particular, considering a MCF with lowly-birefringent (LB) or highly-birefringent (HB) cores, the Monte Carlo method with S random iterations can be performed in each PCM *"mi"*, which is characterized in a given day j by the following parameters:

- The Monte Carlo s-th iteration identified by the subindex $s = 1,\ldots,S$.
- The number of segments N_m of the core m. Each core segment is identified by the subindex $l = 1,\ldots,N_m$.
- The equivalent refractive index of the *"mi"* PCM ($i = x,y$) of the l-th segment associated with the s-th iteration for the j-th day:

$$n_{mi,j,s\text{-}l}^{(\mathrm{eq})}(z;t)=n_{mi,j,s\text{-}l}(t)\left[1+\frac{d_m}{R_{\mathrm{B},l}}\cos\left(2\pi f_{\mathrm{T},l}z+\theta_0+\theta_m\right)\right], \tag{19}$$

where $n_{mi,j,s\text{-}l}(t)$ describes the temporal birefringence fluctuation of the MCF given by a Gaussian random process as detailed later; θ_0 is the offset of the twist angle of the MCF reference axis at $z = 0$; θ_m is the offset of the twist angle of core m measured from the MCF reference axis as shown in Fig. 3; d_m is the Euclidean distance of core m to the MCF center; and $R_{\mathrm{B},l}$ and $f_{\mathrm{T},l}$ are the bending radius and twist rate in the l-th segment, respectively. It should be noted that the local orientation of the fiber principal axes (given by Eqs. (13) and (19)) is different in each segment as a consequence of the longitudinal changes in the twist rate between adjacent segments. On the other hand, although in the numerical simulations and the experimental work of the next sections we have not considered temporal changes in the bending radius and twist rate, in a real deployed MCF system the environmental factors could induce temporal fluctuations in the bending radius and twist rate of the optical media. In that case, $R_{\mathrm{B},l}$ and $f_{\mathrm{T},l}$ should be regarded as time-dependent variables. In addition, the temporal birefringence fluctuation $|n_{my,j,s\text{-}l}(t) - n_{mx,j,s\text{-}l}(t)|$ of the MCF is modeled by a

Gaussian random process $N(\mu(t),\sigma^2)$ with mean $\mu(t) = \Delta n_{m,j}$ describing the value of the intrinsic linear birefringence in core m and day j, and variance $\sigma^2 = \delta n_{m,l}$ modeling the photo-elastic effect in the l-th segment induced by the macrobend $R_{B,l}$ as [31]:

$$\delta n_{m,l} \approx 0.011 n_m^3 \, d_c^2 \big/ R_{B,l}^2 \,, \tag{20}$$

where n_m is the average value of the material refractive index of core m given by Eq. (14) and d_c is the MCF cladding diameter. Thus, the value $n_{mi,j,s\text{-}l}(t)$ can be calculated in the l-th segment and s-th iteration as ($i = x,y$):

$$n_{mi,\,j,s\text{-}l}(t) \sim n_m \left[1 \pm \frac{1}{2} \mathrm{N}\left(\mu(t) = \Delta n_{m,\,j}, \sigma^2 = \delta n_{m,l} \right) \right]. \tag{21}$$

3.2 Numerical simulations

The numerical analysis of the crosstalk between the PCMs was performed in line with the MCF simulation model detailed in previous subsection. Two different 150 m homogeneous two-core fibers (TCFs) comprising LB and HB cores were considered in the numerical simulations, as depicted in Fig. 4. The number of simulated segments and the average value of the linear birefringence in each core $<\Delta n_{m,j}>$ is indicated in Table 1.

We have assumed cores a and b with different birefringence average value and a different number of segments in the LB-TCF case, in order to compare the simulation results with the crosstalk behavior observed in the experimental measurements of the next section. As it is experimentally verified, the higher the birefringence average value $<\Delta n_{m,j}>$ is assumed in a given core m, the lower is the number of segments N_m that should be considered. Additional MCF parameters employed were: $d_{ab} = 36$ μm, $d_c = 125$ μm, $R_0 = 4$ μm, $n_a = n_b = 1.45$, $n_c = 1.44$, $\theta_0 = 0$, and $\lambda = 1550$ nm. Although in a real LB-MCF the core radius R_0 can also present longitudinal fluctuation, it is a less time-consuming approach to consider the longitudinal fluctuation of this fiber parameter as manufacturing imperfections encoded by $<\Delta n_{m,j}>$ in each core $m = a,b$. In HB-MCFs with elliptical cores, the intrinsic birefringence can also be included in $<\Delta n_{m,j}>$ assuming R_0 as the average value of the minor and major axis dimensions.

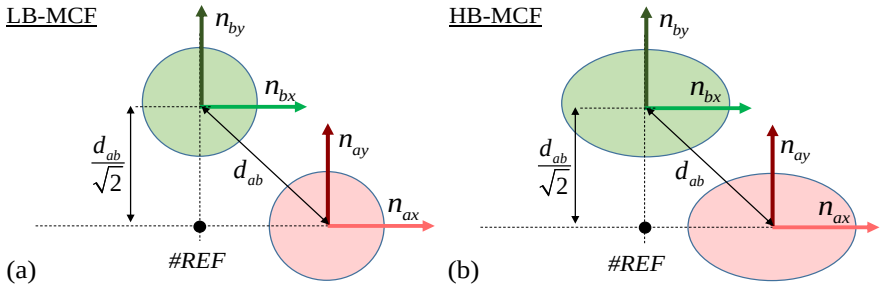

Fig 4. Schematic cross-sections of multi-core fibers simulated: (a) lowly- and (b) highly-birefringent cores.

Table 1. Number of segments and linear birefringence average values considered in the analysis

TCF Parameters	Number of segments N_m		Linear birefringence average value $<\Delta n_{m,j}>$	
Cores	LB	HB	LB	HB
a	8	1	$5 \cdot 10^{-7}$	$4 \cdot 10^{-4}$
b	6	1	$1.2 \cdot 10^{-6}$	$4 \cdot 10^{-4}$

Figure 5 shows the simulation results of the iC-XT, DIC-XT and XIC-XT mean between the PCMs in the LB-TCF of Fig. 4(a) when varying the linear birefringence value $\Delta n_{a,j}$ and $\Delta n_{b,j}$ throughout a 10-day period ($j = 1,\ldots,10$). Following [12,13], the crosstalk mean from a PCM ξ to a PCM υ is defined as $\mu_{\upsilon,\xi} := \mathrm{E}[P_\upsilon(z=L)/P_\xi(z=L)]$, where $\mathrm{E}[\cdot]$ is the expectation

operator, L is the MCF length and $(\upsilon,\xi) \in \{ax,ay,bx,by\}^2$. Monte Carlo method was performed over 100 iterations (S = 100) considering a constant bending radius of R_B = 100 cm along the MCF. In addition, two different twist rate average values of f_T = 0.05 and 1 turns/m were assumed with Gaussian random fluctuations between adjacent segments around ~0.02 turns/m in both cases. The simulation results are shown in Figs. 5(a1)−5(c1) and Figs. 5(a2)−5(c2) for each twist rate average value, respectively. The temporal fluctuation of the linear birefringence $\Delta n_{m,j}$ (m=a,b) depicted in Figs. 5(a1) and 5(a2) was calculated from a Gaussian distribution N(<$\Delta n_{m,j}$>,10^{-7}) considering a similar evolution in both cores in coherence with the experimental results of the next section.

As we can notice from Figs. 5(a1) and 5(a2), the higher the linear birefringence $\Delta n_{m,j}$, the lower the iC-XT mean observed in a given core m. The main reason for this comes from the higher phase mismatching between the intra-core PCMs $LP_{01,mx}$ and $LP_{01,my}$. If the linear birefringence $\Delta n_{m,j}$ increases, the phase mismatching between both orthogonal polarizations increases reducing the iC-XT mean. Furthermore, increasing the fiber twisting from 0.05 to 1 turns/m, the iC-XT mean is also increased in both cores due to the increment of the circular birefringence, as it is observed when comparing the iC-XT levels in Figs. 5(b1) and 5(b2). Note that, as the global birefringence (linear+circular) increases and prevails over the temporal random birefringence fluctuation (~10^{-7}), the temporal fluctuation of the iC-XT mean decreases. This is confirmed by the results for core b in Fig. 5(b2) (with a minimal excursion of 2 dB) and by the experimental measurements presented in the next section.

On the other hand, as depicted in Figs. 5(c1) and 5(c2), the XIC-XT mean presents the same temporal evolution as the iC-XT mean indicating that XIC-XT is mainly generated by the intra-core mode coupling, as it was pointed out in Section 2. Thus, the XIC-XT mean is lower than the DIC-XT mean when the iC-XT mean of both cores is lower than 0 dB. However, increasing the fiber twisting from 0.05 to 1 turns/m, the iC-XT mean increases higher than 0 dB in core a the 1st, 3rd,5th, 6th and 8th days. As a result, the XIC-XT mean is higher than DIC-XT these days, as shown in Fig. 5(c2).

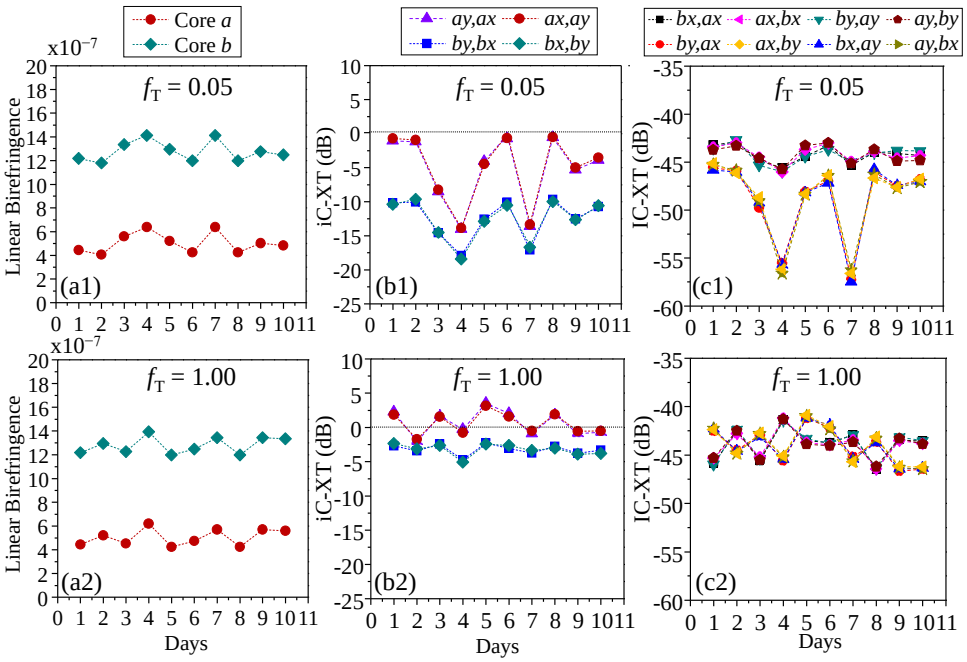

Fig. 5. Simulation results of the crosstalk behavior between the polarized core modes in a 150 m two-core fiber with lowly-birefringent cores, considering the temporal fluctuation of the linear birefringence of each core with a twist rate value of f_T = 0.05 and 1 turns/m: (a) Simulated linear birefringence evolution in cores a and b throughout a 10-day period; (b) intra-core crosstalk evolution; and (c) direct and cross inter-core crosstalk evolution. (iC-XT: intra-core crosstalk, IC-XT: inter-core crosstalk).

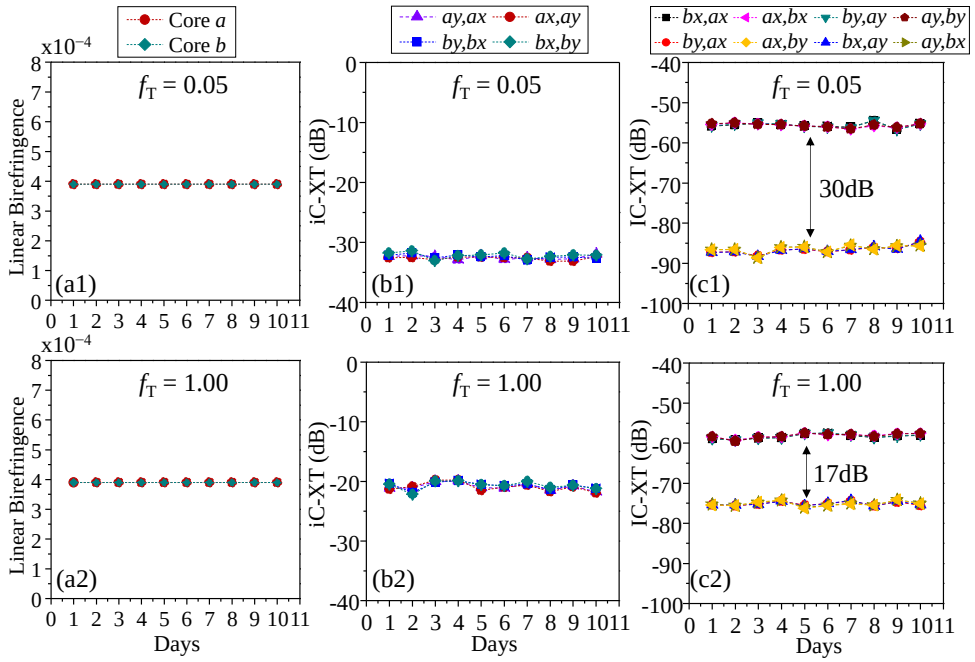

Fig. 6. Simulation results of the crosstalk behavior between the polarized core modes in a 150 m two-core fiber with highly-birefringent cores considering the temporal fluctuation of the linear birefringence of each core with a twist rate value of f_T = 0.05 and 1 turns/m: (a) Simulated linear birefringence evolution in cores *a* and *b* throughout a 10-day period; (b) intra-core crosstalk evolution; and (c) direct and cross inter-core crosstalk evolution. (iC-XT: intra-core crosstalk, IC-XT: inter-core crosstalk).

Figure 6 shows the simulated results considering the 150 m HB-TCF depicted in Fig. 4(b) with an average value of the linear birefringence of $<\Delta n_{m,j}> = 4\cdot10^{-4}$ in both cores ($m = a,b$), as indicated in Table 1. The crosstalk behavior in the HB-TCF was also calculated over 100 iterations assuming the same bending and twisting conditions as in the LB-TCF. Figures 6(a1)−6(c1) and Figs. 6(a2)−6(c2) show the simulated results for twist rate average values of f_T = 0.05 and 1 turns/m, respectively.

It should be noted from Figs. 6(a1) and 6(a2) that we cannot observe a significant temporal birefringence fluctuation, since the temporal random fluctuation of $\Delta n_{m,j}$ was assumed to be of the same order as in the LB cores (around 10^{-7}), much lower than the linear birefringence average value of $<\Delta n_{m,j}> = 4\cdot10^{-4}$ in the HB cores. Therefore, the temporal evolution of the iC-XT mean was found approximately similar in both cores with a maximal excursion of 1 dB, approximately. In addition, note that the iC-XT mean is much lower than in LB cores due to a higher mismatching between the refractive index of the intra-core PCMs. However, increasing the fiber twisting from 0.05 to 1 turns/m the iC-XT mean increases from −33 dB to −20 dB, as shown in Figs. 6(b1) and 6(b2). Considering the low average value and temporal fluctuation of iC-XT in both cores *a* and *b*, the XIC- is lower than DIC-XT for both f_T values, as shown in Figs. 6(c1) and 6(c2). Nevertheless, when the average value of the fiber twist rate increases from 0.05 to 1 turns/m, the difference between DIC- and XIC-XT mean is reduced from +30 to +17 dB due to the increment of the iC-XT mean in both elliptical cores.

An additional comment on the results of Figs. 5 and 6 is in order. The mode coupling from the PCM ξ to PCM υ is the same as from υ to ξ, with $(\upsilon,\xi) \in \{ax,ay,bx,by\}^2$. This is to be expected when operating with a large bending radius R_B, for which the condition $\Delta\phi_{\xi\upsilon} \approx \Delta\phi_{\upsilon\xi}$ can be inferred from Eqs. (18) and (19) for both LB-and HB-MCFs.

In order to further analyze the longitudinal MCF random perturbations induced by MCF bending and twisting, a multi-parameter simulation of the CLMT was performed over 80 Monte Carlo iterations considering a 2 m LB-TCF with cores *a* and *b* comprising a single segment with the same birefringence average value of $<\Delta n_{aj}> = <\Delta n_{bj}> = 10^{-7}$. The temporal

birefringence fluctuation of the TCF was omitted in this simulation. The numerical results are shown in Fig. 7.

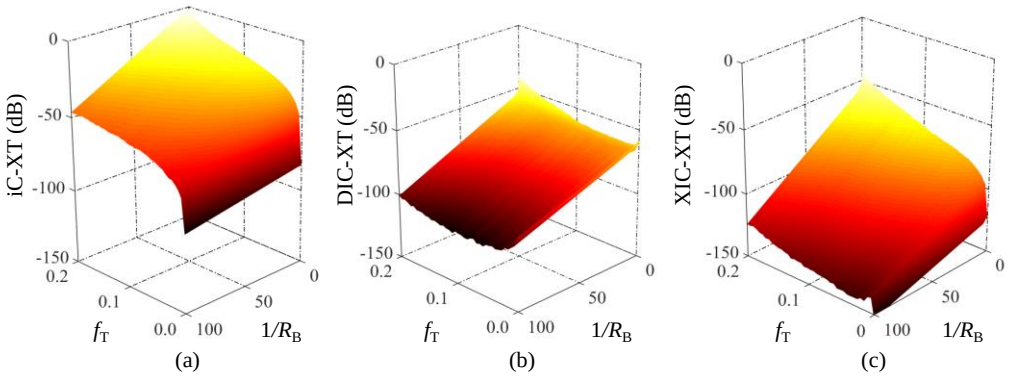

Fig. 7. Multi-parameter simulation of the crosstalk between polarized core modes varying the bending radius ($1/R_B$) and the twist rate (f_T) in a 2 m homogenous two-core fiber with lowly-birefringent cores. (a) intra-core crosstalk mean *ay-ax*, (b) direct inter-core crosstalk mean *bx-ax*, and (c) cross inter-core crosstalk mean *by-ax*.

Figure 7 depicts the mean of: iC-XT *ay-ax* (similar to *by-bx* when assuming cores with similar birefringence), DIC-XT *bx-ax* and XIC-XT *by-ax* when changing the bending radius R_B and fiber twisting conditions f_T. As it can be noticed from Fig. 7(a), we cannot observe intra-core mode coupling between *ax-ay* with $f_T = 0$ in 2 m of LB-TCF. Macrobending increases the phase mismatching between the PCMs *ax* and *ay* without inducing iC-XT due to the photo-elastic effect [31]. As a result, significant XIC-XT cannot be observed for short MCF lengths when $f_T = 0$, as in the case of Fig. 7(c). Nevertheless, an average level of DIC-XT between −100 and −50 dB can be noted from Fig. 7(b) in non-twisting conditions depending on the bending radius value. In addition, the higher the twist rate and the bending radius, the higher the iC-, DIC- and XIC-XT mean due to the reduction of the phase mismatching between the different PCMs of the TCF. Note that DIC- and XIC-XT means are balanced when the iC-XT mean achieves the value of 0 dB in Fig. 7(a). Therefore, MCF twisting can be proposed as a potential strategy for birefringence management to balance the inter-core crosstalk between the different PCMs for short MCF distances. For MCF distances of several kilometers, the iC-XT mean increases and the difference between the mean of the DIC- and XIC-XT are reduced.

Finally, we analyze the crosstalk behavior between the PCMs when operating in nonlinear regime. To this end, we simulated a LB-TCF with fiber parameters: L = 5 m, $f_T = 0.08$, $R_B = 100$ cm, $N_m = 2$ segments, $S = 80$ iterations, d_{ab} = 36 μm, d_c = 125 μm, $R_0 = 4$ μm, $n_a = n_b = 1.45$, $n_c = 1.44$, and λ =1550 nm, with a constant birefringence value in each core of $\Delta n_{a(b),j} = 10^{-7}$ (omitting temporal fluctuation). The power launch level injected into the PCM *ax* was increased from 0 to 40 dBm. The behavior of the mean of the iC-XT (*ay-ax*), DIC-XT (*bx-ax*) and XIC-XT (*by-ax*) is shown in Fig. 8.

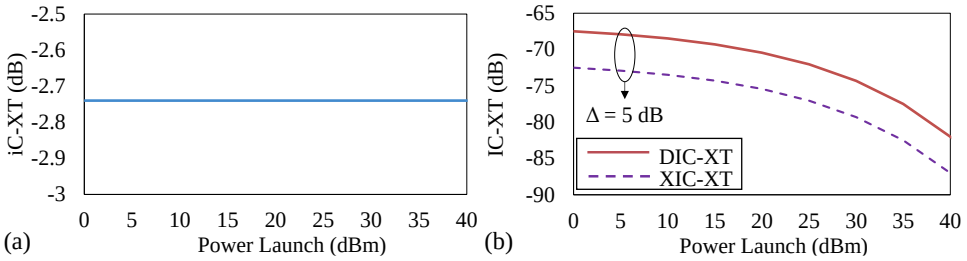

Fig. 8. Numerical results of the nonlinear crosstalk evolution considering a theoretical range of the power launch level in the *ax* polarized core mode in a homogeneous 5 m lowly-birefringent two-core fiber: (a) nonlinear intra-core crosstalk mean between *ay-ax*, and (b) nonlinear direct and cross inter-core crosstalk mean between *bx-ax* and *by-ax*. (iC-XT: intra-core crosstalk, DIC-XT: direct inter-core crosstalk, XIC-XT: cross inter-core crosstalk).

It should be noted from Fig. 8(a) that the iC-XT mean remains unchanged for a power launch level $P_L = P_{ax}(z=0)$ lower than 40 dBm. Therefore, we conclude that the nonlinear birefringence induced by the nonlinear polarization $\boldsymbol{P}^{(3)}$ in Eqs. (4) does not increase the iC-XT when considering realistic optical power levels. Moreover, as shown in Fig. 8(b), the mean of DIC- and XIC-XT is reduced as the power launch level increases. This is because the Kerr effect detunes the phase constants of PCMs between different cores, as reported in [12]. Furthermore, the difference between the DIC- and XIC-XT mean is constant around 5 dB when the optical power launch increases, due to the constant behaviour of the iC-XT in the nonlinear regime.

4. Experimental results

In order to validate the theoretical analysis of the previous sections, experimental measurements are performed on a homogeneous four-core fiber (4CF) analyzing the temporal birefringence fluctuation of the optical media and its impact on the mean of the linear and nonlinear crosstalk between the PCMs. The employed experimental set-up is shown in Fig. 9.

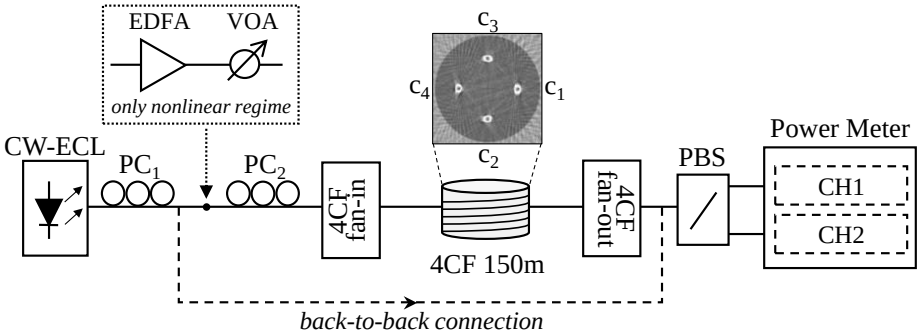

Fig. 9. Experimental set-up for intra- and inter-core crosstalk evaluation between the polarized core modes of cores 1 and 3 of a four-core fiber (4CF), considering multi-core fiber temporal birefringence fluctuation and both linear and nonlinear power regimes.

A tunable continuous-wave external cavity laser (CW-ECL) at 1550 nm with a linewidth of 50 kHz was used along with two polarization controllers (PC_1 and PC_2). The first polarization controller (PC_1) was employed to align the polarization axes of the CW-ECL and the polarization beam splitter (PBS) in a back-to-back (B2B) connection, as detailed in Fig. 9. A polarization analyzer (Optellios PS2300) was used to verify that the output light of the PC_1 was linearly polarized along the *x* axis by maximizing the upper branch of the PBS in the B2B connection. The second polarization controller (PC_2) was inserted to modify the polarization launched into a given core of the 4CF. The additional erbium doped fiber amplifier (EDFA) followed by a variable optical attenuator (VOA) was employed only for the nonlinear crosstalk analysis between the PCMs. A 3D fan-in/fan-out device with 2.2 dB insertion losses was employed in order to inject and extract the optical power launched into a 150 m homogeneous single-mode 4CF Fibercore SM-4C1500(8.0/125) spooled on a reel with a constant bending radius of 100 cm and constant twist rate of 1 turns/m inside a methacrylate box to reduce the external perturbations. In addition, the laboratory room was isolated and the air cushions were inflated in our active optical table to minimize the external perturbations induced by human activity.

The crosstalk behavior between the PCMs of cores 1 and 3 was analyzed in the linear and nonlinear regime by injecting into a given PCM an optical power launch level of 0 dBm and 6 dBm, respectively. In the nonlinear regime, the EDFA gain was maximized in order to reduce the crosstalk averaging due to amplified spontaneous emission (ASE) noise, as recommended in [12], and the power launch was controlled by the VOA. The optical power of the two PCMs ($LP_{01,mx}$ and $LP_{01,my}$) of a given core *m* (with $m = 1,3$) was separated with the PBS and measured with a power meter comprising two different channels (Thorlabs PM320E).

The mean of the linear and nonlinear iC-, DIC- and XIC-XT between the PCMs of cores 1 and 3 was estimated using the wavelength sweeping method [10,12] from 1540 to 1590 nm with 5 pm step. The CW-ECL was previously tested between 1540 and 1590 nm to confirm that the polarization remains unchanged when sweeping the laser wavelength. It should be noted that the wavelength sweeping method can also be used to estimate the value of the linear birefringence of each core in different days, as detailed in [32,33]. Moreover, it should be remarked that the impact of the dispersive effects and the inter-core skew effect on the time dependence of the crosstalk [6,27] was minimized using a CW-ECL with a reduced linewidth of 50 kHz. As it was experimentally verified, considering that the linear birefringence of each core remains unchanged during more than 10 hours, we analyzed the temporal birefringence fluctuation by performing measurements at different days and months.

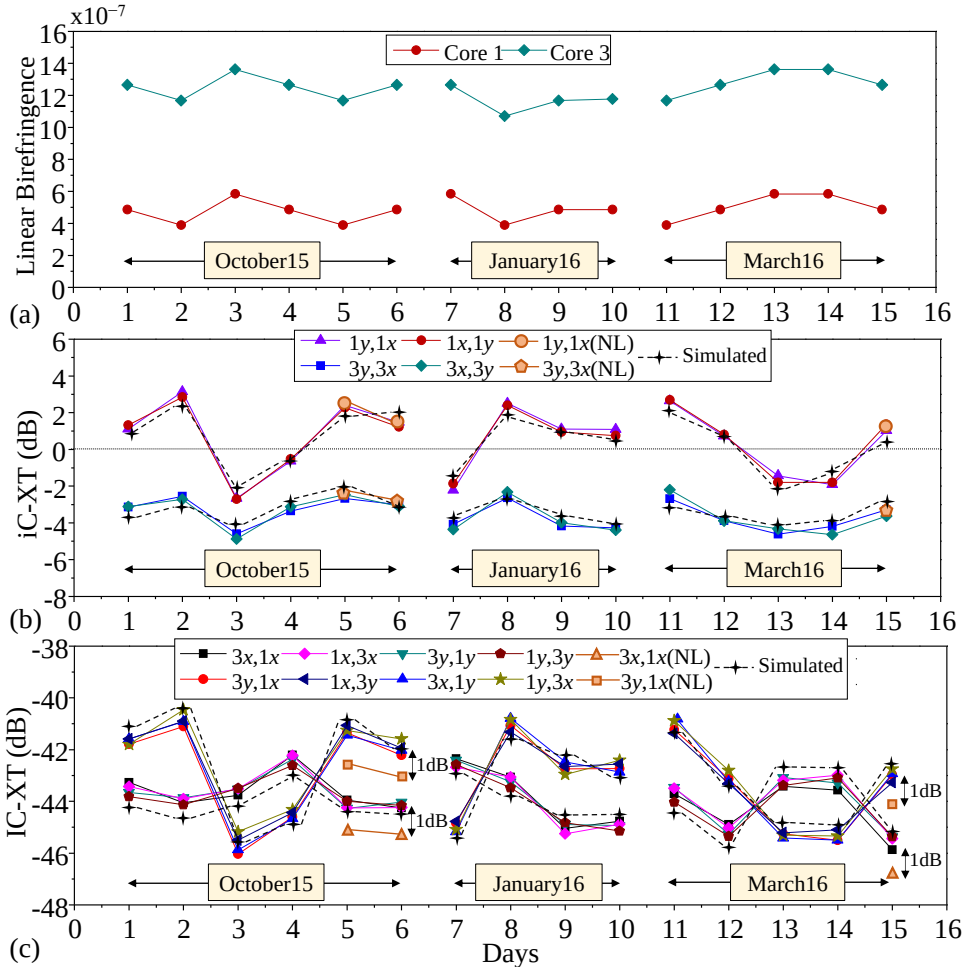

Fig. 10: Experimental results of the temporal linear birefringence fluctuation over different days and months of a 150 m 4CF, and corresponding intra- and inter-core crosstalk mean between cores 1 and 3. A power launch level of P_L = 0 dBm was used in linear regime (NL: nonlinear regime with P_L = 6 dBm). (a) Linear birefringence evolution of cores 1 and 3, (b) intra-core crosstalk 1*x*-1*y* and 3*x*-3*y*, and (c) direct- and cross-inter-core crosstalk 1*i*-3*j* with *i*,*j* = *x*,*y*

Figure 10 shows the temporal fluctuation of the linear birefringence and the crosstalk mean behavior between the PCMs of cores 1 and 3 measured in six consecutive days in October 2015, four consecutive days in January 2016, and five consecutive days in March 2016, with similar temperature conditions in the laboratory set-up. As shown in Fig. 10(a), cores 1 and 3 present a different average value of the linear birefringence estimated to be $\langle \Delta n_{1,j} \rangle = 4.9 \cdot 10^{-7}$ and $\langle \Delta n_{3,j} \rangle = 1.2 \cdot 10^{-6}$, respectively. It can be noted that the average value

of the linear birefringence is constant in each core the three different measured months. Moreover, although the average value of the linear birefringence is different in each core, the temporal evolution of the linear birefringence presents a similar shape in both cores, in line with our assumptions in Section 3.

As depicted in Figs. 10(a) and (b), the higher the linear birefringence in a given core, the lower the mean of the iC-XT. Furthermore, it should be noted that iC-XT in core 3 is lower than in core 1 due to a higher mismatching between the orthogonal polarizations. In line with the simulations of Section 3, the iC-XT mean presents a lower temporal fluctuation in the more birefringent core (core 3), which occurs when the average value of the birefringence is higher than the temporal random birefringence fluctuation ($\sim 10^{-7}$). In addition, we can observe from Fig. 10(c) that the temporal evolution of the XIC-XT mean presents the same behavior as the iC-XT mean, indicating that XIC-XT depends directly on the iC-XT of both cores. As a result, DIC-XT is higher than XIC-XT when iC-XT is lower than 0 dB in both cores, as it was observed the 3rd and 4th days (October 2015), the 7th day (January 2016), and the 13th and 14th days (March 2016). Furthermore, the experimental measurements of Fig. 10 fit correctly with the CLMT simulation when using Eqs. (17)-(21) with the parameters indicated in Table 1 for the LB-TCF with $N_1 = N_a = 8$, $N_3 = N_b = 6$ and assuming a temporal birefringence $\Delta n_{1,j} = \Delta n_{a,j}$ and $\Delta n_{3,j} = \Delta n_{b,j}$ as depicted in Fig. 10(a). Therefore, we conclude that the more birefringent a given core is, the lower number of segments should be used to simulate the crosstalk between the PCMs, as was pointed out in Section 3.

On the other hand, the nonlinear crosstalk between de PCMs 1*y*-1*x*, 3*y*-3*x*, 3*x*-1*x* and 3*y*-1*x* was also measured the 5th, 6th and 15th days with a power level of 6 dBm launched into the corresponding PCM, taking into account the insertion losses of 2.2 dB of the 3D fan-in device. As it was previously observed in Section 3, the iC-XT mean presents the same value in nonlinear regime considering that the nonlinear birefringence can be neglected for realistic optical power launch levels lower than 40 dBm. In addition, the DIC- and XIC-XT mean is reduced around 1 dB keeping constant the difference between both inter-core crosstalk types as a direct consequence of the constant behavior of the iC-XT mean in nonlinear regime.

Moreover, although the crosstalk analysis between the PCMs is restricted only to cores 1 and 3, the linear birefringence $\Delta n_{m,j}$ was also measured in cores 2 and 4. The average value of the linear birefringence of cores 2 and 4 was found to be $\langle \Delta n_{2,j} \rangle \approx \langle \Delta n_{4,j} \rangle \approx 7 \cdot 10^{-7}$. In addition, the average value of the iC-XT mean of each core was analyzed as a function of the average value of the linear birefringence $\langle \Delta n_{m,j} \rangle$ including a numerical simulation of the CLMT.

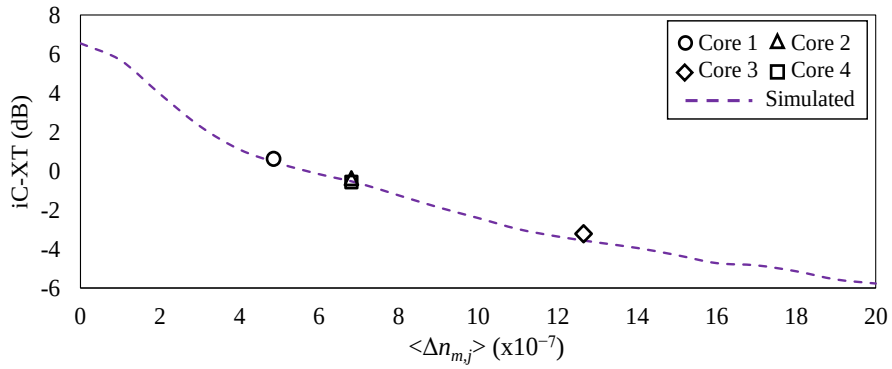

Fig. 11: Experimental measurement and simulated results of the intra-core crosstalk (iC-XT) mean evolution with the average value of the linear birefringence. Solid points: measured data of cores 1, 2, 3, 4 in a 150 m homogeneous four-core fiber. Dashed line: simulation results using the coupled-local mode equation, Eq. (17).

Figure 11 shows the experimental and simulated results of the iC-XT mean evolution when increasing the average value of the linear birefringence $\langle \Delta n_{m,j} \rangle$ in a given core using Eqs. (17)-(21) considering 80 Monte Carlo iterations. It was assumed a core *m* with the fiber parameters of the 4CF Fibercore SM-4C1500(8.0/125): $n_m = 1.452$, $n_c = 1.444$, $\lambda = 1550$ nm,

d_{ab} = 36 μm, d_c = 125 μm. The distance to the reference center of the 4CF is fixed at $d_m = d_{ab}/\sqrt{2}$ = 25.46 μm. The bending radius and the twist rate was assumed with a similar value as in the experimental set-up with R_B = 100 cm and f_T = 1 turns/m, respectively. It can be noted that the iC-XT mean is reduced when the average value of the linear birefringence $<\Delta n_{m,j}>$ increases inducing a higher phase mismatching between orthogonal polarizations. Furthermore, it was confirmed that the simulated results fit correctly with the experimental measurements of each core, validating the theoretical analysis reported in previous sections.

The experimental analysis reported in this section addresses a non-real deployed SM-MCF system with constant bending and twisting conditions. For real deployed MCF systems, the results herein presented should be refined by considering the multimode regime, higher fiber distances and random bending radius and twist rate along the fiber length. Furthermore, the polarization-mode dispersion (PMD) and the inter-core skew should also be investigated in real deployed MCF systems. To this end, distributed and lumped analytical models can be proposed in MCF media as in standard single-mode systems [34,35]. Alternatively, the CLMT can also be employed to evaluate the impact of the longitudinal and temporal fiber perturbations on the statistics of the PMD.

5. Conclusions

In this paper, we have reported the theoretical and experimental analysis of the intra- and inter-core crosstalk behavior in SM-MCF including the temporal and longitudinal birefringence perturbations of the optical media. In order to propose an accurate analytical model, the coupled local-mode theory was derived from the Maxwell equations including both temporal and longitudinal MCF birefringence perturbations in the phase functions and MCCs of the polarized core modes. Two new MCCs $m_{ax,ay}(z;t)$ and $\eta_{ax,by}(z;t)$ were found modeling iC-XT and XIC-XT, respectively. The theoretical analysis shows that $\eta_{ax,by}$ coefficient can be neglected indicating that the XIC-XT mean depends directly on the iC-XT mean observed in both cores *a* and *b*, as it was verified numerically and experimentally.

In addition, a MCF simulation model of the CLMT was proposed and validated experimentally including both longitudinal and temporal birefringent effects in the equivalent refractive indexes $n_{mi}^{(eq)}$. The numerical simulations comprising LB and HB cores indicate that the higher is the linear birefringence in a given core, the lower is the value and the temporal fluctuation of the iC-XT mean. Furthermore, the XIC-XT mean presents the same temporal evolution as the iC-XT mean indicating that XIC-XT is mainly generated due to intra-core mode coupling. As a result, the XIC-XT mean is lower than the DIC-XT mean when the iC-XT mean of both cores is lower than 0 dB. Both DIC- and XIC-XT are balanced when iC-XT mean achieves the value of 0 dB in each core. Hence, MCF twisting was proposed as a birefringence management strategy in short MCF distances to balance the DIC- and XIC-XT. However, when higher MCF distances of several kilometers are considered, the iC-XT mean increases reducing the difference between the mean of the DIC- and XIC-XT. In nonlinear regime it was observed that the nonlinear iC-XT mean remains unchanged when the power level launched into a given polarized core mode increases. In contrast, the DIC- and XIC-XT mean is reduced in nonlinear regime showing a similar evolution. Finally, extensive experimental measurements performed in three different months using a homogeneous 4CF confirm the crosstalk behavior observed in the numerical simulations between the PMCs. The experimental validation also pointed out that the temporal linear birefringence evolution is similar in different cores of the optical media.

Appendix: calculation of the transversal local eigenfunctions $F_{mi}(x,y;z,t)$

The transversal local eigenfunction F_{mi} for the PCM *"mi"* can be calculated using the closed-form expressions detailed in [23] for the LP_{01} mode in the cores and cladding regions. However, considering that the local eigenfunction depends on the longitudinal and temporal MCF random perturbations, it should be calculated as a function of the equivalent refractive index $n_{mi}^{(eq)}$ detailed in Section 3. Therefore, the eigenfunction $F_{mi}(r;z,t)$ can be expressed in a local polar coordinate system (r,φ,z) of a given core *m* as:

$$F_{mi}(r;z,t)=\begin{cases} J_0\left(\dfrac{u_{mi}(z;t)}{R_0}r\right)\Big/J_0\left(u_{mi}(z;t)\right); & r\le R_0 \\ K_0\left(\dfrac{w_{mi}(z;t)}{R_0}r\right)\Big/K_0\left(w_{mi}(z;t)\right); & r>R_0 \end{cases}, \tag{22}$$

where $r = (x^2+y^2)^{1/2}$; R_0 is the core radius (assuming all cores of the MCF with identical radius); u_{mi} and w_{mi} are the modal parameters of the PCM *"mi"*, which can be calculated as:

$$u_{mi}(z;t)=\left(1+\sqrt{2}\right)V_{mi}(z;t)\Big/\left[1+\left(4+V_{mi}^4(z;t)\right)^{1/4}\right], \tag{23a}$$

$$w_{mi}(z;t)=\sqrt{V_{mi}^2(z;t)-u_{mi}^2(z;t)}, \tag{23b}$$

and $V_{mi}(z;t)$ is the normalized frequency of the PCM *"mi"*:

$$V_{mi}(z;t)=k_0R_0C_F\sqrt{\left(n_{mi}^{(eq)}(z;t)\right)^2-n_c^2}, \tag{24}$$

with $n_{mi}^{(eq)}$ given by Eq. (19), C_F an auxiliary parameter referred as the correction factor and n_c the material refractive index of the cladding. The correction factor C_F is included in Eq. (24) to calculate the correct values of the normalized frequency when using the nominal value of the core radius. It is worth mentioning that in real SMFs and MCFs, the core radius presents longitudinal variations along the fiber length, as was pointed out previously in Section 3. In order to consider these core radius fluctuations, we have included in Eq. (24) the correction factor C_F, which should be calculated using the cut-off wavelength (λ_C) of the fiber as a reference. Specifically, the correction factor is found as $C_F = 0.7$ in Section 3.2 and $C_F = 0.9$ in Section 4 (λ_C = 1410 nm). Moreover, note that in Eq. (24) it was assumed the same material refractive index of the cladding for the *x* and *y* polarization axes.

Funding and Acknowledgments

This work has been partly funded by Spain National Plan project MINECO/FEDER UE XCORE TEC2015-70858-C2-1-R; HIDRASENSE RTC-2014-2232-3; European Regional Development Fund (ERDF) and the Galician Regional Government under project GRC2015/018. A. Macho and M. Morant work was supported by BES-2013-062952 F.P.I. Grant and postdoc UPV PAID-10-14 program, respectively.